
AN EXTREME WAVE FIELD IN THE WINTER ANTARCTIC MARGINAL ICE ZONE DURING AN EXPLOSIVE POLAR CYCLONE

A PREPRINT

Alberto Alberello*
The University of Tokyo, Japan

Luke G. Bennetts
University of Adelaide, Australia

Miguel Onorato
Università di Torino & INFN, Italy

Marcello Vichi
University of Cape Town, South Africa

Keith MacHutchon
University of Cape Town, South Africa

Clare Eayrs
New York University Abu Dhabi, UAE

Butteur Ntamba Ntamba
Cape Peninsula University of Technology, South Africa

Alvise Benetazzo
Istituto di Scienze Marine, Consiglio Nazionale delle Ricerche, Italy

Filippo Bergamasco
Università Ca' Foscari, Italy

Filippo Nelli
Swinburne University of Technology, Australia

Rohinee Pattani
Atkins, UK

Hans Clarke
The University of Melbourne, Australia

Alessandro Toffoli
The University of Melbourne, Australia

March 1, 2025

ABSTRACT

Propagation of energetic surface gravity waves over a > 40 km transect of the winter Antarctic marginal ice zone comprised of pancake floes and interstitial frazil ice during an explosive polar cyclone are presented, obtained with a shipborne stereo-camera system. The waves are shown to attenuate at an exponential rate over distance, but, despite this, remain large, even at the deepest measurement locations and in 100% ice concentration, where they are up to 8 m in amplitude—the largest waves measured in comparable conditions. The occurrence of large waves in the marginal ice zone is shown to be consistent with linear theory. Using concomitant measurements of wind speeds, evidence is given that wind-to-wave momentum transfer occurs through a 100% pancake/frazil ice cover, which is not permitted in most contemporary models.

1 Introduction

The marginal ice zone (MIZ) is the region of the ocean where surface gravity waves and sea ice interact [1, 2]. In winter, when sea ice extent reaches its maximum, the MIZ (defined by ice concentration between 15% and 80%) occupies 20–30% of the total sea ice area [3] and consists mostly of small (1–10 m diameter), thin (order 0.1 m thickness), roughly circular, pancake ice floes and interstitial frazil ice [2]. Pancake-dominated MIZs are highly mobile and rapidly evolve in response to the frequent intense storms and cyclones in the winter Southern Ocean [4]. Moreover, they are associated with rapid ice production, as the unconsolidated mix of thin ice keeps the ocean in closer contact with the cold atmosphere than the thicker, consolidated inner pack ice [5].

*Corresponding author: alberto.alberello@outlook.com.

Pancake floes are formed in wavy conditions [6], and, once formed, waves prevent pancakes from consolidating [7]. Therefore, it is important to understand how the large waves that characterise the Southern Ocean propagate through the winter Antarctic MIZ, and whether strong winds over the MIZ transfer momentum to waves. A key unknown is the attenuation rate of large-amplitude waves over distance through a pancake/frazil ice cover, as this informs predictions of the width of the ice-covered region impacted by waves and hence the MIZ extent [8]. Moreover, the evolution of the wave spectrum through the MIZ, particularly the reduction in amplitudes, frequency downshifting and directional spread, are required to predict the floe size distribution [9]. Momentum transfer from winds over the ice cover is a prominent knowledge gap, with most contemporary models simply assuming wind energy input is identical to the open ocean but scaled by the fraction of the ocean surface not covered by sea ice, i.e. no wave generation in 100% ice concentration [10, 11].

Despite advances over the past decade in measuring wave propagation through the Arctic [12] and Antarctic MIZ [13, 14], there is a lack of measurements in the harsh winter Antarctic MIZ and for the extreme sea states in the winter Southern Ocean, where, over the open ocean, the mean significant wave height in many sectors reaches 5 m and the 90th percentiles (extremes) are up to 7 m [15]. In the Arctic, an array of wave buoys was used to measure wave propagation through an autumn MIZ consisting of 50–100% concentration pancake/frazil ice, during a storm event where the incident significant wave height from the open ocean was up to 5 m [16]. Large waves (significant wave heights > 3 m) were found to attenuate at a linear rate, and small waves (< 3 m) at an exponential rate. In the Southern Ocean, arrays of wave buoys were used to measure waves in the Antarctic MIZ during spring to early winter, in which floes were 10–100 m in diameter, ≈ 0.5 m thick and covered a range of concentrations [17]. Significant wave heights in excess of 6 m were recorded, but only in ice concentration $\approx 50\%$ in the outskirts of the MIZ (within the first few tens of kilometres from the ice edge).

Stereo-imaging techniques have emerged as a tool for in-situ wave measurements in the MIZ. The images are used to reconstruct the sea surface elevation in time and space, thus enabling analysis of wave dynamics in both two-dimensional physical space and the frequency–direction spectral domain, including statistical analysis of the wave field [18]. Remote sensing techniques have also been developed to measure the directional wave spectrum in the MIZ [19]. Airborne SAR configurations can provide robust directional spectra over 60–80 km long transects of the MIZ [20, 21]. However, stereo-imaging, being an in-situ technique, can be used to simultaneously measure sea ice geometrical properties [22] and can be combined with co-located meteorological measurements, e.g. wind velocities.

To date, use of stereo-imaging techniques for wave measurements in sea ice has been limited in scope. Campbell et al. [23] and Smith and Thomson [24] both use stereo-camera systems to derive one-dimensional wave spectra and bulk wave properties (peak periods and significant wave heights) from images over small domains (order 100 m^2) for small waves propagating through pancake ice. Campbell et al. [23] use a camera system on a fixed platform on the edge of a lake, whereas Smith and Thomson [24] use a camera system on a moored vessel in the Arctic MIZ, and hence have to correct the images for wave-induced ship motions.

In this Letter, we address the gap in measurements of large waves in the winter Antarctic MIZ. Stereo-camera measurements are presented of extreme sea states ($\approx 90\text{th}$ percentile for the sector at the ice edge) during an explosive polar cyclone along an > 40 km transect into the Antarctic MIZ closely aligned with the mean wave direction ($\approx 30^\circ$ difference). Large individual wave events are recorded in the MIZ, even in 100% ice concentration at the deepest measurement locations, notwithstanding the exponential attenuation of wave energy with distance. The occurrence of large waves is shown to be consistent with linear wave theory. Evidence is given of momentum transfer from winds over the first 40 km into the MIZ, which could explain the milder attenuation rate than previously reported for high ice concentrations. Analysis of the wave spectra reveals frequency downshifting of the dominant wave energy, which is attributed to stronger attenuation of high-frequency components by the ice cover and evolution of the incident wave field from the open ocean, and broadening of the directional spectrum.

2 Field Measurements

Between 07:00 and 08:00 UTC on the 4th July 2017, the South African icebreaker S.A. Agulhas II entered the Antarctic MIZ (62° South and 30° East) during an intense polar cyclone [4]. Ice concentration on the day, sourced from AMSR2 satellite at 3.125 km resolution [25], is shown in Fig. 1a. The icebreaker moved South encountering the ice edge at 08:00 UTC, i.e. the northernmost location where sea ice concentration exceeds 10% in a 1 km radius around the vessel (ASPeCt; [26]). It reached 100% sea-ice concentration at 09:00 UTC (Fig. 1a), approximately 10 km from the ice edge, after which it continued South, whilst remaining in 100% ice concentration [22]. Over this time, intense cyclonic conditions (wind speed $18\text{--}19\text{ m s}^{-1}$ from NW, turning by $< 10^\circ$ during the measurements) intensified ocean waves at the ice edge, from 6.7 m at 08:00 UTC to 7.8 m at 13:00 UTC [27], therefore exceeding the 90th percentile of waves in the Indian sector of Southern Ocean, noting that it is the sector containing the most intense waves in

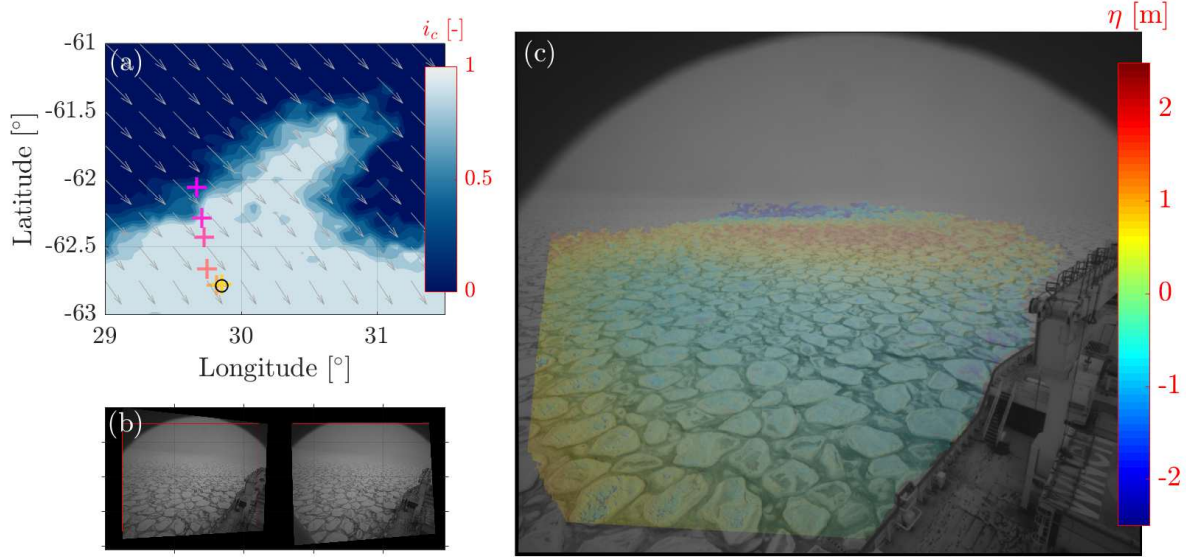


Figure 1: (a) Overview of study area with ice concentration from AMSR2 on the 4th July 2017 and wind vectors from ERA5 at 11:00 UTC, with crosses denoting average location of wave measurements during a 30 mins acquisition and the circle location of wave measurements obtained by a buoy deployed on an ice floe during the voyage [28]. (b) Pair of synchronised camera images, and (c) reconstructed surface elevation, η .

the Southern Ocean [15]. The mean wave direction at the ice edge was aligned with the wind and directional spread remained steady [27].

A system of two GigE monochrome industrial CMOS cameras with a 2/3 inch sensor was installed on the monkey bridge of the icebreaker ≈ 34 m from the waterline and with their axes 5 m apart, tilted 20° below the horizon. The cameras were equipped with 5 mm lenses to provide a field of view of the ocean surface $\approx 90^\circ$ around the port side of the ship (Fig. 1b). Images were recorded with resolution 2448×2048 pixels and a sampling rate 2 Hz during daylight on the 4th July (from 07:00 to 14:00 UTC). Acquisition was performed over ≈ 30 mins intervals (≈ 6 times longer than Smith and Thomson [24]).

The wave acquisition stereo-camera system (WASS; [29]) is used to reconstruct the water surface elevation. Camera images are first calibrated to remove lens distortion and find the pixel to meter conversion factor. The algorithm detects and matches common features in each pair of synchronised images, allowing three-dimensional reconstruction of the free surface (Fig. 1c). The WASS system captures $\approx 150 \text{ m} \times 200 \text{ m}$ snapshots of the ocean surface (≈ 5 times larger than Smith and Thomson [24]). The system operated from 07:00 to 14:00 UTC but images acquired in the early hours of the day (07:00–08:00 UTC) lacked contrast and light to reconstruct sea surface elevation. An inertial measurement unit (IMU) installed close to the cameras and synchronised with the camera images is used to correct for ship motions and reconstruct the surface elevation with respect to a common horizontal plane defining the mean sea level.

The sea surface elevation is reconstructed in a frame of reference moving with the ship, and, therefore, is affected by Doppler shift. The wave spectrum is retrieved by computing the directional spectrum in the ship frame of reference with the wavelet method [30] using timeseries extracted on a virtual array, i.e. at multiple points within the field of view, and then correcting the directional spectrum for Doppler shift using the dispersion relation from linear wave theory and deep water conditions [31]. The two-dimensional frequency–direction spectra, $E(f, \theta)$, are subsequently integrated with respect to direction to give one-dimensional frequency spectra, $E(f)$.

WASS was also used to monitor in-situ ice properties along the transect. Remotely sensed concentration varied from 0% at 08:00 UTC to 100% at 09:00 UTC. In-situ measurements revealed that from 09:00 UTC onwards the sea ice cover was comprised of $\approx 60\%$ pancake ice floes, with median diameter 3.1 m, and the remaining $\approx 40\%$ interstitial frazil ice [22].

3 Results

Surface elevation timeseries around the largest waves recorded (H_{\max} ; maximum crest to trough distance) at the six locations denoted by crosses in Fig. 1a are shown in Fig. 2a, where d denotes distance from the ice edge projected along the mean wave direction. The first timeseries (top panel) was obtained close to the ice edge ($d = 5$ km) in $\approx 50\%$ ice concentration. Subsequent timeseries are obtained deeper into the MIZ ($d \geq 15$ km) in 100% ice concentration. The significant wave height, i.e. $H_S = 4\sigma_\eta$ where σ_η is the surface elevation standard deviation, is also shown for each timeseries (Fig. 2a; dashed lines).

The significant wave height close to the ice edge is 6.6 m (Fig. 2a top panel). It is approximately the same as ERA5 reanalysis in open water just outside the ice edge (ERA5 only provides wave data up to 15% ice concentration). The significant wave height decreases deeper into the MIZ, to $H_S = 4.6$ m at $d = 44$ km (bottom panel). The value at this location agrees with co-located buoy measurements (black circle in Fig. 1a; [4]).

At each location, the largest wave is found as part of an energetic wave group. The maximum wave height also tends to diminish with distance into the MIZ. But large waves, $H_{\max} \approx 8$ m, are recorded in 100% ice concentration 43 km into the MIZ (second to bottom panel). To our knowledge, this is the largest recorded wave in 100% ice concentration. The maximum to significant wave height ratio (H_{\max}/H_S) slightly increases over distance, from 1.3 close to the edge to 1.5 deeper in the MIZ, but remains lower than the rogue wave threshold, $H_{\max}/H_S = 2$ [32]. Fig. 2b shows the probability density function of the normalised wave intensity ($\eta^2/\langle\eta^2\rangle$). The exponential distribution associated to a linear (Gaussian) sea surface elevation is shown for reference [33].

The significant wave height (normalised by its open water counterpart) decays exponentially with distance d (Fig. 2c) at a rate $\alpha \approx 8 \times 10^{-6} \text{ m}^{-1}$. For comparison, significant wave heights versus distance into the Antarctic MIZ based on buoy measurements [17] are also shown in Fig. 2b for high ice concentration ($> 80\%$; red) and low ice concentration ($< 80\%$; green), which have attenuation rates $26.5\text{--}32.7 \times 10^{-6} \text{ m}^{-1}$ and $1.6\text{--}5.0 \times 10^{-6} \text{ m}^{-1}$, respectively. In both cases, the lower attenuation is for long waves ($T_p > 14$ s; thick dashed) while the higher for short waves ($T_p \leq 14$ s; thin dashed).

The two- and one-dimensional spectra, i.e. $E(f, \theta)$ and $E(f)$, at the six locations are shown in Fig. 3a–Fig. 3b. The peak period (the most energetic period; T_p) and the mean period (the reciprocal frequency moment of the wave spectrum; T_m) at each location are indicated on the one-dimensional spectra (Fig. 3b), along with the corresponding open ocean peak period ($T_{p, \text{ERA5}}$) and mean period ($T_{m, \text{ERA5}}$) at the ice edge at the time of the measurement and accounting for advection time. The open ocean peak and mean periods increase from $T_{p, \text{ERA5}} = 12.4$ s and $T_{m, \text{ERA5}} = 10.4$ s when the measurements were made at the ice edge to $T_{p, \text{ERA5}} = 13.5$ s and $T_{m, \text{ERA5}} = 11.4$ s when the measurements were made at $d = 43\text{--}44$ km. The values of T_p and T_m at $d = 43\text{--}44$ km agree with co-located buoy measurements (Fig. 3b), and at the ice edge with open ocean values.

Attenuation of wave energy with distance into the MIZ is evident in the one-dimensional spectra, with higher frequencies (shorter periods) experiencing greater attenuation than lower frequencies (longer periods). The attenuation, combined with the increasing peak and mean periods over time at the ice edge, causes the peak and mean periods to increase over distance and time. The peak period increases by only a small amount between $d = 5$ km and $d = 36$ km, from $T_p = 12.0$ s to $T_p = 12.6$ s. Beyond $d = 36$ km, it increases sharply to $T_p = 15.1$ s at 43–44 km. In contrast, T_m increases steadily over distance, from 10.3 s at $d = 5$ km to 12.9 s at $d = 43\text{--}44$ km. The difference in the evolution of the peak and mean periods is attributed to the dependence of the peak period on spectral resolution, whereas the mean period, being an integral over frequencies, is a more robust parameter. Attenuation causes the peak and mean periods at the deepest locations ($d = 43\text{--}44$ km) to be 12–15% longer than the corresponding open ocean peak and mean periods.

The spectral bandwidths (the breadth of the spectrum in frequency evaluated at half of the spectral peak energy, Δf ; [32]) are indicated by horizontal bars on the one-dimensional spectra in Fig. 3b. They show narrowing of the spectrum with distance into the MIZ, with the bandwidth at $d = 43\text{--}44$ km $\approx 80\%$ of the bandwidth at the ice edge.

The two-dimensional spectra (Fig. 3a) indicate the directional properties of the spectrum also evolve in the MIZ. Close to the ice edge (top panel), the wave spectrum is bimodal, with two distinct energy peaks of comparable magnitude $\approx 25^\circ$ from each other with the lower-frequency peak a swell and the higher-frequency peak a wind sea locally generated. At the next measurement point ($d = 15$ km), the spectrum is dominated by one energy peak, i.e. it is unimodal, which is attributed to wave transformation, e.g. refraction, caused by the local conformation of the intermediate ice concentration area West of the transect (see Fig. 1a). The spectrum remains unimodal until the deepest measurement locations ($d = 43\text{--}44$ km), where some small additional peaks appear. The frequency averaged directional spread, i.e. a measure of the directional distribution of wave energy [16], is indicated by vertical bars for each location. Directional spread tends to increase over distance, from $\approx 40^\circ$ at $d = 5$ km to $\approx 60^\circ$ at $d = 43\text{--}44$ km, but the trend is not well

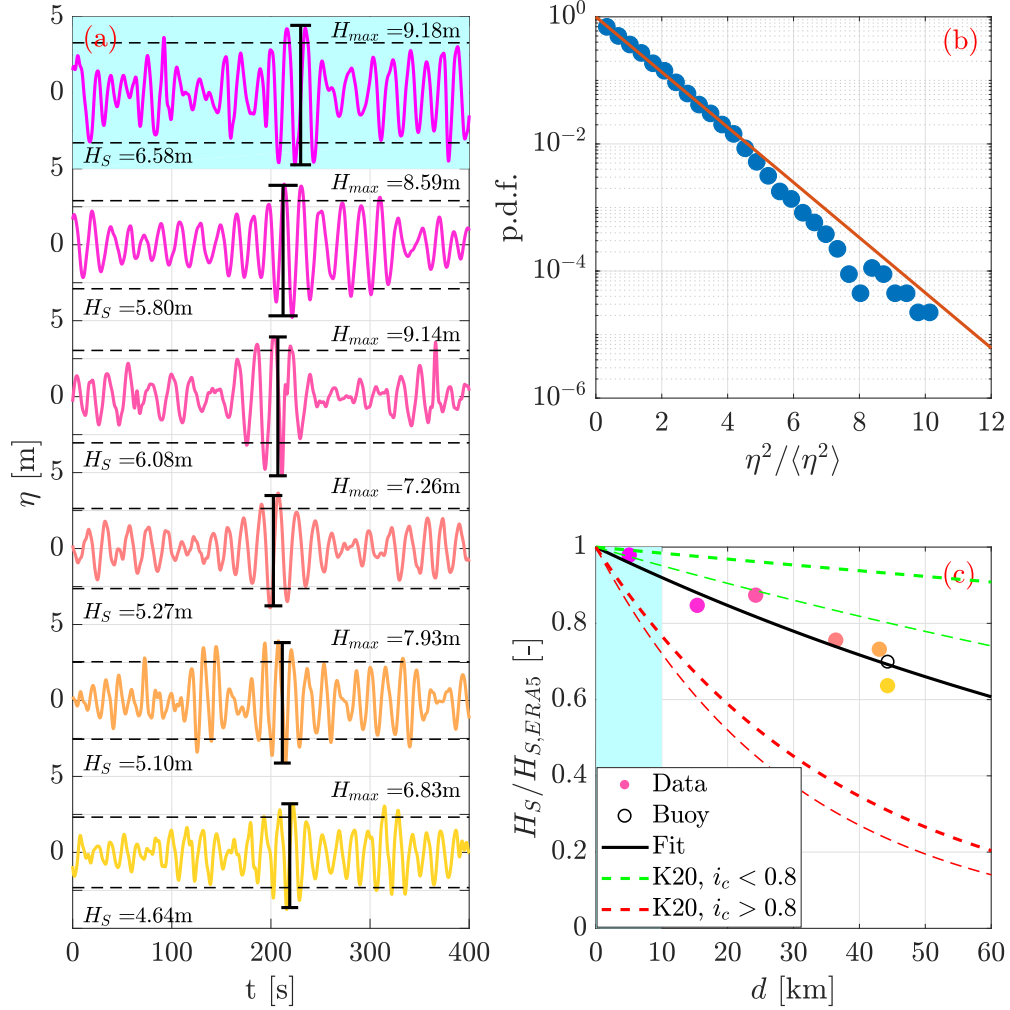


Figure 2: (a) Samples of surface elevation time series at progressive distances from the ice edge (top-to-bottom; color-coding corresponds to location shown in Fig. 1a) shown around the highest wave in the record. Dashed lines indicate H_S and cyan background denotes intermediate ice concentration. (b) Probability density function of the wave intensity, where red line indicates linear wave theory benchmark. (c) Evolution of H_S with distance from the ice edge. Dots are present data (cross the buoy) and gray line denotes best (exponential) fit. Dashed lines are attenuation derived from Kohout et al. [17] for $i_c < 0.8$ (green; thicker for $T_p > 14$ s) and $i_c > 0.8$ (red; thicker for $T_p > 14$ s).

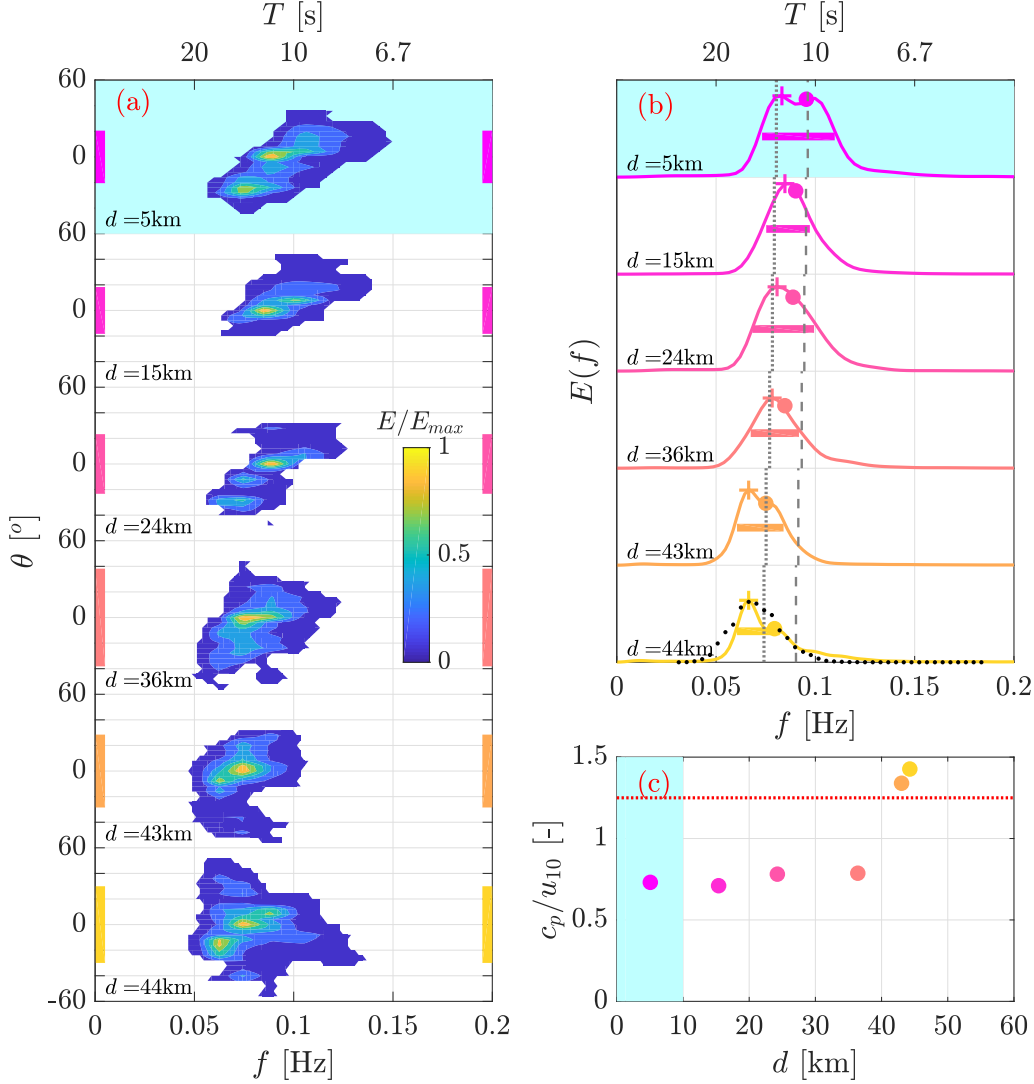


Figure 3: (a) Two-dimensional and (b) one-dimensional wave spectra at progressive distances from the ice edge (top-to-bottom; color-coding corresponds to the locations shown in Fig. 1a). Two-dimensional spectra are normalised by the peak energy to highlight directional properties, and one-directional spectra are normalised by a common factor to highlight energy loss. In (a), Cartesian coordinates are used as the spectra cover only a narrow directional range, $-60^\circ < \theta < 60^\circ$, and bars denote directional spread (σ_0). In (b), bars denote spectral bandwidth, crosses and dots peak and mean period (T_p ; T_m), dotted and dashed grey lines peak and mean period in open ocean ($T_{p,ERA5}$; $T_{m,ERA5}$). In the bottom panel, the spectrum from the buoy is also shown (black dotted). (c) Wave age at progressive distances from the ice edge. Dotted line denotes the threshold between young and old waves. In (a–c), cyan backgrounds denote the measurement location in intermediate ice concentration.

defined, and the maximum is $\approx 75^\circ$ at $d = 36$ km. The directional spread agrees with typical open water values during storms in the Southern Ocean [34].

The ratio c_p/u_{10} , where c_p is the phase velocity (ratio of wavelength to wave period) and u_{10} the wind speed, is known as the wave age [35]. It is used to separate young waves, which are growing in size and length under the action of wind ($c_p/u_{10} < 1.25$), from old (swell) waves, which propagate without active wind input ($c_p/u_{10} > 1.25$). The wave age (Fig. 3c), computed using wind speed from the onboard met-station, indicate waves are young over the first ≈ 40 km of the MIZ ($c_p/u_{10} \approx 0.75$), but sharply switch to old ($c_p/u_{10} \approx 1.40$) at the deepest two measurement locations ($d = 43$ – 44 km), caused by the sudden drop in wind speed (from ≈ 25 m s $^{-1}$ to ≈ 17 m s $^{-1}$).

4 Discussion and Conclusions

The exponential attenuation of significant wave height with distance into the Antarctic MIZ is consistent with the recent findings of Kohout et al. [17]. However, the attenuation rate found here is ≈ 4 times less than the attenuation rate Kohout et al. [17] report for high ice concentrations, and slightly greater than the rate they report for low ice concentrations. The differences indicate the attenuation rate depends on ice cover properties, as Kohout et al. [17] used measurements when the MIZ was comprised of floes 10–100 m in diameter, whereas the measurements reported here were taken when the MIZ was comprised of small pancake ice floes (1–10 m) and interstitial frazil ice. For small pancake floes in the Arctic (diameters ≈ 0.3 m) interspersed with water and/or grease ice, significant wave height attenuation rates have not been reported, but attenuation rates at the frequency corresponding to peak periods reported here are of the order 10^{-6} – 10^{-5} m^{-1} [36, 37].

The low attenuation rate found herein for the winter MIZ corresponds to significant wave heights halving every ≈ 75 km, e.g. $H_S = 8.5$ m in open ocean remains $H_S > 0.5$ m at 300 km in the ice-covered ocean, preventing floe welding and maintaining an unconsolidated ice cover [6, 28]. Thus, during the passage of intense storms and cyclones, wave–ice interactions are likely to persist hundreds of kilometres in from the ice edge, even in 100% ice concentration. This finding corroborates satellite observations by Stopa et al. [38] spanning multiple seasons of waves propagating hundreds of kilometers into the Antarctic MIZ.

Most models scale wind input according to the open water fraction [10, 39], i.e. no wind input in 100% ice concentration. In contrast, Rogers et al. [11] suggest wind energy transfer can occur in ice-covered regions, particularly in frazil, brash and/or pancake ice fields, albeit less effectively than in the open water. Moreover, Zhao and Zhang [40] recently presented a theoretical model in which wind can actively transfer energy to waves through the ice cover. The wave age values presented here (Fig. 3c) indicate strong winds potentially feed wave growth in 100% ice concentration for tens of kilometres into a pancake/frazil MIZ. Wind input would offset wave attenuation due to the ice cover, providing an alternative explanation for the lower attenuation rate than reported by Kohout et al. [17], noting Kohout et al. [17] do not report the prevailing winds during their measurements.

Few measurements of the directional wave spectrum exist in the MIZ, with most using buoys, which can be unreliable [16, 17], and some using airborne SAR [20, 21]. There is no consensus on the evolution of the directional spectrum in the MIZ. Previous measurements in MIZs consisting of floes much smaller than wavelengths (e.g. pancake floes), range from narrowing [16, 21] to no change [41] to broadening [1, 42, 20]. The measurements presented here show evidence of directional broadening. The physical mechanism responsible for the broadening is unknown, noting that theoretical models generally predict directional narrowing due to wave dissipation in a MIZ consisting of small floes [43].

Attenuation of wave energy over distance into the MIZ reduces the wave steepness ($\varepsilon = k_p H_S / 2$, where k_p is the wavenumber associated to T_p) from 0.10 at $d = 5$ km to 0.04 at $d = 43$ –44 km. Despite the large waves measured (Fig. 2a), the small steepness values in the MIZ indicate wave probabilities should conform to linear wave predictions [44], which is backed by the similarity between the probability density function and the linear wave theory benchmark (Fig. 2b). The finding is in agreement with observations by Thomson et al. [45] in the Arctic MIZ for milder wave conditions. Our measurements strengthens the argument that nonlinear wave mechanisms responsible for the generation of large waves (e.g. modulational instability) are weakened in the MIZ. Note, however, there is no theoretical framework for wave nonlinearity in the MIZ at present, as it is defined only for waves in the open ocean [32].

In conclusion, measurements have been reported of extreme wave conditions in the winter Antarctic MIZ during an explosive polar cyclone, which were captured by a stereo-camera system over a 44 km transect. The findings from the measurements have implications for the treatment of wave–ice interactions in wave and sea ice forecasting models. In particular, most contemporary models tend to dissipate wave energy over short distances in 100% ice concentration regardless of the ice type, whereas evidence has been presented to support dependence of attenuation rates on ice type, and that waves can propagate long distances into MIZs consisting of pancake–frazil ice even at 100% ice concentration. As a consequence, the width of the winter Antarctic MIZ is likely to be under-predicted by an order of magnitude, especially if a concentration-based MIZ definition is used, as in many coupled models [46] and studies [3, 47], for which the MIZ width would have been only ≈ 10 km during the reported observations. Consequently, heat and momentum exchanges promoted by wave-induced motion in 100% sea ice are likely to be poorly represented in models at present [48, 42, 49, 9].

Acknowledgments

The expedition was funded by the South African National Antarctic Programme through the National Research Foundation. This work was motivated by the Antarctic Circumnavigation Expedition (ACE) and partially funded by the

ACE Foundation and Ferring Pharmaceuticals. AA, LB and AT were supported by the Australian Antarctic Science Program (project 4434). AA is supported by the Japanese Society for the Promotion of Science (PE19055). LGB is supported by the Australia Research Council (FT190100404). LGB and AT are supported by the Australia Research Council (DP200102828). MO was supported from the Simons Collaboration on Wave Turbulence, Award No. 617006, and from the “Departments of Excellence 2018–2022” Grant awarded by the Italian Ministry of Education, University and Research (MIUR, L.232/2016). MV and KM were supported by the NRF SANAP contract UID118745. CE was supported under NYUAD Center for global Sea Level Change project G1204. We are indebted to Captain Knowledge Bengu and the crew of the SA Agulhas II for their invaluable contribution to data collection. ERA5 reanalysis was obtained using Copernicus Climate Change Service Information. MO acknowledges B GiuliNico for interesting discussions. AA, AT and MO thank L Fascette for technical support during the cruise.

Datasets for this research (reconstructed surface elevations) are available through the Australian Antarctic Data Centre (AADC): Alberello et al. (2021) Wave acquisition stereo-camera system measurements (WASS) from a voyage of the S.A. Agulhas II, July 2017, Ver. 1, Australian Antarctic Data Centre – doi:10.26179/q9bd-5f74.

References

- [1] Peter Wadhams, Vernon A. Squire, J. A. Ewing, and R. W. Pascal. The effect of the marginal ice zone on the directional wave spectrum of the ocean. *Journal of Physical Oceanography*, 16(2):358–376, 1986.
- [2] P. Wadhams, G. Aulicino, F. Parmiggiani, P. O. G. Persson, and B. Holt. Pancake ice thickness mapping in the Beaufort sea from wave dispersion observed in SAR imagery. *Journal of Geophysical Research: Oceans*, 2018.
- [3] J. C. Stroeve, S. Jenouvrier, G. G. Campbell, C. Barbraud, and K. Delord. Mapping and assessing variability in the antarctic marginal ice zone, pack ice and coastal polynyas in two sea ice algorithms with implications on breeding success of snow petrels. *The Cryosphere*, 10(4):1823–1843, 2016.
- [4] Marcello Vichi, Clare Eayrs, Alberto Alberello, Anriëtte Bekker, Luke Bennetts, David Holland, Ehlke de Jong, Warren Joubert, Keith MacHutchon, Gabriele Messori, Jhon F. Mojica, Miguel Onorato, Clinton Saunders, Sebastian Skatulla, and Alessandro Toffoli. Effects of an explosive polar cyclone crossing the Antarctic marginal ice zone. *Geophysical Research Letters*, 0(0), 2019.
- [5] M. J. Doble. Simulating pancake and frazil ice growth in the Weddell Sea: A process model from freezing to consolidation. *Journal of Geophysical Research: Oceans*, 114(C9), 2009.
- [6] Hayley H. Shen, Stephen F. Ackley, and Mark A. Hopkins. A conceptual model for pancake-ice formation in a wave field. *Annals of Glaciology*, 33:361–367, 2001.
- [7] L. A. Roach, M. Smith, and S. Dean. Quantifying growth of pancake sea ice floes using images from drifting buoys. *Journal of Geophysical Research: Oceans*, 2018.
- [8] L. G. Bennetts, S. O’Farrell, and P. Uotila. Impacts of ocean-wave-induced breakup of Antarctic sea ice via thermodynamics in a stand-alone version of the CICE sea-ice model. *The Cryosphere*, 11(3):1035–1040, 2017.
- [9] Lettie A. Roach, Cecilia M. Bitz, Christopher Horvat, and Samuel M. Dean. Advances in modeling interactions between sea ice and ocean surface waves. *Journal of Advances in Modeling Earth Systems*, 11(12):4167–4181, 2019.
- [10] Jingkai Li, Alison L. Kohout, and Hayley H. Shen. Comparison of wave propagation through ice covers in calm and storm conditions. *Geophysical Research Letters*, 42(14):5935–5941, 2015.
- [11] W. Erick Rogers, Michael H. Meylan, and Alison L. Kohout. Estimates of spectral wave attenuation in antarctic sea ice, using model/data inversion. *Cold Regions Science and Technology*, page 103198, 2020.
- [12] Jim Thomson, Stephen Ackley, Fanny Girard-Ardhuin, Fabrice Ardhuin, Alex Babanin, Guillaume Boutin, John Brozena, Sukun Cheng, Clarence Collins, Martin Doble, Chris Fairall, Peter Guest, Claus Gebhardt, Johannes Gemmrich, Hans C. Graber, Benjamin Holt, Susanne Lehner, Björn Lund, Michael H. Meylan, Ted Maksym, Fabien Montiel, Will Perrie, Ola Persson, Luc Rainville, W. Erick Rogers, Hui Shen, Hayley Shen, Vernon Squire, Sharon Stammerjohn, Justin Stopa, Madison M. Smith, Peter Sutherland, and Peter Wadhams. Overview of the Arctic Sea State and Boundary Layer Physics Program. *Journal of Geophysical Research: Oceans*, 123(12):8674–8687, 2018.
- [13] Klaus M. Meiners, Ken M. Golden, Petra Heil, Jan L. Lieser, Rob Massom, Bettina Meyer, and Guy D. Williams. Introduction: Sipex-2: A study of sea-ice physical, biogeochemical and ecosystem processes off east antarctica during spring 2012. *Deep Sea Research Part II: Topical Studies in Oceanography*, 131:1–6, 2016. East Antarctic sea-ice physics and ecosystem processes.

- [14] S. F. Ackley, S. Stammerjohn, T. Maksym, M. Smith, J. Cassano, P. Guest, J.-L. Tison, B. Delille, B. Loose, P. Sedwick, and et al. Sea-ice production and air/ice/ocean/biogeochemistry interactions in the ross sea during the piers 2017 autumn field campaign. *Annals of Glaciology*, 61(82):181–195, 2020.
- [15] Ian R. Young, Emmanuel Fontaine, Qingxiang Liu, and Alexander V. Babanin. The wave climate of the southern ocean. *Journal of Physical Oceanography*, 50(5):1417 – 1433, 2020.
- [16] F. Montiel, V. A. Squire, M. Doble, J. Thomson, and P. Wadhams. Attenuation and directional spreading of ocean waves during a storm event in the autumn beaufort sea marginal ice zone. *Journal of Geophysical Research: Oceans*, 123(8):5912–5932, 2018.
- [17] Alison Kohout, Madison Smith, Lettie A. Roach, Guy Williams, Fabien Montiel, and Michael J. M. Williams. Observations of exponential wave attenuation in antarctic sea ice during the piers campaign. *Annals of Glaciology*, page 1–14, 2020.
- [18] Alvise Benetazzo, Francesco Barbariol, Filippo Bergamasco, Andrea Torsello, Sandro Carniel, and Mauro Sclavo. Stereo wave imaging from moving vessels: Practical use and applications. *Coastal Engineering*, 109:114 – 127, 2016.
- [19] Fabrice Ardhuin, Fabrice Collard, Bertrand Chapron, Fanny Girard-Ardhuin, Gilles Guitton, Alexis Mouche, and Justin E. Stopa. Estimates of ocean wave heights and attenuation in sea ice using the sar wave mode on sentinel-1a. *Geophysical Research Letters*, 42(7):2317–2325, 2015.
- [20] Peter Sutherland and Jean-Claude Gascard. Airborne remote sensing of ocean wave directional wavenumber spectra in the marginal ice zone. *Geophysical Research Letters*, 43(10):5151–5159, 2016.
- [21] Peter Sutherland, John Brozena, W. Erick Rogers, Martin Doble, and Peter Wadhams. Airborne remote sensing of wave propagation in the marginal ice zone. *Journal of Geophysical Research: Oceans*, 123(6):4132–4152, 2018.
- [22] A. Alberello, M. Onorato, L. Bennetts, M. Vichi, C. Eayrs, K. MacHutchon, and A. Toffoli. Pancake ice floe size distribution during the winter expansion of the Antarctic marginal ice zone. *The Cryosphere*, 13(1):41–48, 2019.
- [23] Alexander J. Campbell, Adam J. Bechle, and Chin H. Wu. Observations of surface waves interacting with ice using stereo imaging. *Journal of Geophysical Research: Oceans*, 119(6):3266–3284, 2014.
- [24] Madison Smith and Jim Thomson. Pancake sea ice kinematics and dynamics using shipboard stereo video. *Annals of Glaciology*, page 1–11, 2019.
- [25] A. Beitsch, L. Kaleschke, and S. Kern. Investigating high-resolution AMSR2 sea ice concentrations during the February 2013 fracture event in the Beaufort Sea. *Remote Sensing*, 6(5):3841–3856, 2014.
- [26] Anthony P Worby. *A technique for making ship-based observations of Antarctic sea ice thickness and characteristics*. Number 14. Antarctic CRC, 1999.
- [27] Copernicus Climate Change Service. *ERA5: Fifth generation of ECMWF atmospheric reanalyses of the global climate*. Copernicus Climate Change Service Climate Data Store (CDS), 2017.
- [28] Alberto Alberello, Luke Bennetts, Petra Heil, Clare Eayrs, Marcello Vichi, Keith MacHutchon, Miguel Onorato, and Alessandro Toffoli. Drift of pancake ice floes in the winter antarctic marginal ice zone during polar cyclones. *Journal of Geophysical Research: Oceans*, 125(3):e2019JC015418, 2020.
- [29] Filippo Bergamasco, Andrea Torsello, Mauro Sclavo, Francesco Barbariol, and Alvise Benetazzo. WASS: An open-source pipeline for 3D stereo reconstruction of ocean waves. *Computers & Geosciences*, 107:28 – 36, 2017.
- [30] M. A. Donelan, W. M. Drennan, and A. K. Magnusson. Nonstationary analysis of the directional properties of propagating waves. *Journal of Physical Oceanography*, 26(9):1901–1914, 1996.
- [31] Odd Falinsen. *Sea loads on ships and offshore structures*, volume 1. Cambridge university press, 1993.
- [32] M. Onorato, S. Residori, U. Bortolozzo, A. Montina, and F.T. Arecchi. Rogue waves and their generating mechanisms in different physical contexts. *Physics Reports*, 528(2):47 – 89, 2013. Rogue waves and their generating mechanisms in different physical contexts.
- [33] A. Toffoli, D. Proment, H. Salman, J. Monbaliu, F. Frascoli, M. Dafilis, E. Stramignoni, R. Forza, M. Manfrin, and M. Onorato. Wind generated rogue waves in an annular wave flume. *Phys. Rev. Lett.*, 118(14):144503, 2017.
- [34] M. H. Derkani, A. Alberello, F. Nelli, L. G. Bennetts, K. G. Hessner, K. MacHutchon, K. Reichert, L. Aouf, S. S. Khan, and A. Toffoli. Wind, waves, and surface currents in the southern ocean: Observations from the antarctic circumnavigation expedition. *Earth System Science Data Discussions*, 2020:1–22, 2020.
- [35] Leo H. Holthuijsen. *Waves in Oceanic and Coastal Waters*. Cambridge University Press, 2007.

- [36] W. Erick Rogers, Jim Thomson, Hayley H. Shen, MJ Doble, Peter Wadhams, and Sukun Cheng. Dissipation of wind waves by pancake and frazil ice in the autumn Beaufort Sea. *Journal of Geophysical Research: Oceans*, 121(11):7991–8007, 2016.
- [37] Sukun Cheng, W. Erick Rogers, Jim Thomson, Madison Smith, Martin J. Doble, Peter Wadhams, Alison L. Kohout, Björn Lund, Ola P.G. Persson, Clarence O. Collins III, Stephen F. Ackley, Fabien Montiel, and Hayley H. Shen. Calibrating a viscoelastic sea ice model for wave propagation in the arctic fall marginal ice zone. *Journal of Geophysical Research: Oceans*, 122(11):8770–8793, 2017.
- [38] Justin E. Stopa, Peter Sutherland, and Fabrice Ardhuin. Strong and highly variable push of ocean waves on Southern Ocean sea ice. *Proceedings of the National Academy of Sciences*, 115(23):5861–5865, 2018.
- [39] Qingxiang Liu, W. Erick Rogers, Alexander Babanin, Jiangkai Li, and Changlong Guan. Spectral Modeling of Ice-Induced Wave Decay. *Journal of Physical Oceanography*, 50(6):1583–1604, 05 2020.
- [40] Xin Zhao and Changpeng Zhang. A theoretical model of wind-wave growth over an ice-covered sea. *Boundary-Layer Meteorology*, pages 1–19, 2020.
- [41] Daniel R. Hayes, Adrian Jenkins, and Stephen McPhail. Autonomous underwater vehicle measurements of surface wave decay and directional spectra in the marginal sea ice zone. *Journal of Physical Oceanography*, 37(1):71 – 83, 2007.
- [42] Seth Zippel and Jim Thomson. Air-sea interactions in the marginal ice zone. *Elem Sci Anth*, 4, 2016.
- [43] Vernon A. Squire and Fabien Montiel. Evolution of directional wave spectra in the marginal ice zone: A new model tested with legacy data. *Journal of Physical Oceanography*, 46(10):3121 – 3137, 2016.
- [44] Elmira Fadaeiazar, Justin Leontini, Miguel Onorato, Takuji Waseda, Alberto Alberello, and Alessandro Toffoli. Fourier amplitude distribution and intermittency in mechanically generated surface gravity waves. *Phys. Rev. E*, 102:013106, Jul 2020.
- [45] Jim Thomson, Johannes Gemmrich, W. Erick Rogers, Clarence O. Collins, and Fabrice Ardhuin. Wave groups observed in pancake sea ice. *Journal of Geophysical Research: Oceans*, 2019.
- [46] M. J. Doble and J. R. Bidlot. Wave buoy measurements at the Antarctic sea ice edge compared with an enhanced ECMWF WAM: Progress towards global waves-in-ice modelling. *Ocean Modelling*, 70:166 – 173, 2013. Ocean Surface Waves.
- [47] Courtenay Strong, Dallas Foster, Elena Cherkaev, Ian Eisenman, and Kenneth M. Golden. On the definition of marginal ice zone width. *Journal of Atmospheric and Oceanic Technology*, 34(7):1565–1584, 2017.
- [48] Yuri Hiraike and Motoyoshi Ikeda. Descending surface water at the antarctic marginal ice zone and its contribution to intermediate water: an ice-ocean model. *Journal of oceanography*, 65(5):587–603, 2009.
- [49] Madison Smith and Jim Thomson. Ocean surface turbulence in newly formed marginal ice zones. *Journal of Geophysical Research: Oceans*, 0(ja), 2019.